

# Preparation of AS1411 Aptamer Modified Mn-MoS<sub>2</sub> QDs for Targeted MR Imaging and Fluorescence Labelling of Renal Cell Carcinoma

This article was published in the following Dove Press journal:  
*International Journal of Nanomedicine*

Shaohui Zheng<sup>1-3,\*</sup>  
Min Zhang<sup>2,\*</sup>  
Hongyan Bai<sup>2</sup>  
Meijuan He<sup>2</sup>  
Lina Dong<sup>2</sup>  
Lulu Cai<sup>2</sup>  
Mingming Zhao<sup>2</sup>  
Qi Wang<sup>2</sup>  
Kai Xu<sup>1-3</sup>  
Jingjing Li<sup>1-3</sup>

<sup>1</sup>Department of Radiology, Affiliated Hospital of Xuzhou Medical University, Xuzhou 221006, People's Republic of China; <sup>2</sup>School of Medical Imaging, Xuzhou Medical University, Xuzhou 221004, People's Republic of China; <sup>3</sup>Institute of Medical Imaging and Digital Medicine, Xuzhou Medical University, Xuzhou 221004, People's Republic of China

\*These authors contributed equally to this work

**Background:** Early diagnosis of renal cell carcinoma is extremely significant for the effective treatment of kidney cancer. The development of AS1411 aptamer modified Mn-MoS<sub>2</sub> QDs provides a promising fluorescence/magnetic resonance (MR) dual-modal imaging probe for the precise diagnosis of renal clear cell carcinoma.

**Methods:** In this work, Mn-MoS<sub>2</sub> QDs were synthesized through a simple “bottom-up” one-step hydrothermal method. AS1411 aptamer was modified on the Mn-MoS<sub>2</sub> QDs to improve the specificity to renal cell carcinoma. The characteristics of Mn-MoS<sub>2</sub> QDs were confirmed by transmission electronic microscopy (TEM), atomic force microscope (AFM), X-ray photoelectron spectrometer (XPS), photoluminescence (PL) emission spectra, etc. Cellular fluorescence labelling was investigated using the Mn-MoS<sub>2</sub> QDs and AS1411-Mn-MoS<sub>2</sub> QDs. The T<sub>1</sub>-weighted MR imaging was assessed by the in vitro MR cell imaging and in vivo MR imaging. Finally, the long-term toxicity of Mn-MoS<sub>2</sub> QDs was investigated by the hematology and histological analysis.

**Results:** The prepared Mn-MoS<sub>2</sub> QDs exhibited excellent aqueous property, intense fluorescence, low toxicity, high quantum yield of 41.45% and high T<sub>1</sub> relaxivity of 16.95 mM<sup>-1</sup>s<sup>-1</sup>. After conjugated with AS1411 aptamer, the AS1411-Mn-MoS<sub>2</sub> QDs could specifically fluorescently label the renal carcinoma cells and present a specific MRI signal enhancement in the tumor region of mice bearing renal carcinoma tumors. Furthermore, Mn-MoS<sub>2</sub> QDs revealed low toxicity to the mice via hematology and histological analysis.

**Conclusion:** These results demonstrated the potential of AS1411-Mn-MoS<sub>2</sub> QD as a novel nanoprobe for targeted MR imaging and fluorescence labelling of renal cell carcinoma.

**Keywords:** manganese-doped molybdenum disulfide quantum dots, renal cell carcinoma, magnetic resonance imaging, cell fluorescence labelling

## Introduction

Cancer has been a major public concern and a serious threat to health across the world. It is estimated that a total of 18.1 million new cancer cases and 9.6 million cancer deaths will occur worldwide in 2018.<sup>1</sup> Kidney cancer accounted for 3.3% among the new cases and the incidence has increased globally in recent years. Specially, renal cell carcinoma is the main type and occupies approximately 90–95% of all kidney neoplasm. Unfortunately, about 30% of the renal cell carcinoma patients showed metastatic disease upon its diagnosis, thus, aggravating the mortality of the renal cell carcinoma patients.<sup>2</sup> Therefore, early diagnosis for the cancer is extremely important to greatly increase the chances for effective treatment of renal cell carcinoma.<sup>3</sup>

Correspondence: Jingjing Li; Kai Xu  
Email qingchao0124@163.com;  
xkpaper@163.com

Recently, multimodal imaging has attracted tremendous attention as an effective diagnosis strategy for the early detection of cancer.<sup>4</sup> The integration of several imaging techniques allows precise and fast diagnosis by acquiring the comprehensive information of the tissues through the signals of the synergistic-multiplexed imaging, including fluorescence imaging, photoacoustic imaging (PA), magnetic resonance imaging (MRI), computed tomography imaging (CT), etc.<sup>5–7</sup> Among them, MRI has revealed many advantages in the non-invasive diagnosis by producing high 3D spatially resolved images of the tissues with a deep penetration.<sup>5–8</sup> On the other hand, fluorescence imaging (FL) is highly sensitive, thus could be applied for qualitative or quantitative studies of biological behaviors in molecular or cellular levels, which could compensate for the disadvantages of MRI.<sup>9</sup> Therefore, the combination of FL and MRI would maximize their advantages and provide an effective approach for the localization of cancer.<sup>7,10</sup>

Normally, gadolinium (Gd) has been widely used as the contrast agent attributed to the excellent contrast effect in  $T_1$ -weighted imaging.<sup>11</sup> However, as reported, the Gd contained contrast agents may cause a rare but extremely severe disease, nephrogenic fibrosis.<sup>12</sup> Therefore, a special contrast agent without Gd is also needed to address this issue. Fortunately, manganese (Mn) element could also produce similar contrast enhancement in  $T_1$ -weighted imaging ascribed to its five unpaired 3d electrons.<sup>13</sup> On the other hand, Mn is also an essential element of physiological metabolism, and its homeostasis can be effectively regulated by the *in vivo* biological system, enabling its potential application in MRI.<sup>14</sup> However, as previous reports, the Mn element in its free form may cause apparent neurotoxicity in the mice and rat study. For example, the aqueous Mn(II) has been found to impart neurotoxicity with an  $LD_{50}$  in mice of 0.3 mmol/kg injected intravenously and 1.0 mmol/kg injected intraperitoneally. Therefore, various approaches were used to tackle the problem associated with free Mn by preparing chelated manganese, hybrid manganese agents, macromolecular agents, and nanoparticle-based agents to mask the free manganese.<sup>15</sup>

In recent years, quantum dots (QDs) have been studied for their size-dependent optical and electronic properties attributed to the bandgap widening when the dimensions of QDs are reduced below the exciton Bohr radius of the material.<sup>16</sup> To date, various quantum dots have been prepared as fluorescent probes, including graphene QDs, semiconductor QDs, carbon dots, polymer dots, etc.<sup>16–18</sup>

However, most of these QDs exhibited strong cell toxicity and low stability, hindering their applications in the biomedical fields.<sup>19</sup> Recently,  $MoS_2$  QDs have been identified as a promising QD nanomaterial candidate attributed to its high stability, low toxicity, abundance and unique optical and electronic properties.<sup>20</sup> For example, Zhou et al prepared a  $MoS_2$  QD for long-term tracking of living cells.<sup>21</sup> Lin et al synthesized a  $MoS_2$  QD with size-dependent tunable photoluminescence for real-time optical cellular imaging.<sup>22</sup> These as-prepared  $MoS_2$  QDs were generally developed via a “top-down” route to engineer the size and dimension of bulk  $MoS_2$  powder. However, the “top-down” method always required high-powered sonication, long reaction time and hazardous organic solvents.<sup>23</sup> Very recently, a “bottom-up” hydrothermal method has attracted great attention for the facile synthesis of  $MoS_2$  QDs.<sup>24</sup> Typically,  $MoS_2$  QDs could be produced via one-step with different sulfur and molybdenum as precursors. For example, Gu et al fabricated water-soluble  $MoS_2$  QDs via a one-step hydrothermal method as a fluorescent probe for hyaluronidase detection.<sup>24</sup>

Recently, metallic atoms were also employed to dope in the 2D  $MoS_2$  nanomaterials to improve their properties.<sup>25</sup> Tan et al substituted Mn atoms into the  $MoS_2$  nanosheet by supercritical hydrothermal reaction to create the intrinsic ferromagnetism.<sup>26</sup> Se atoms were doped into the  $MoS_2$  nanosheet to enhance the catalytic performance by the increasing number of active sites and enhanced conductivity.<sup>27</sup> However, to date, to the best of our knowledge, the Mn-doped  $MoS_2$  QDs have not been investigated for MR imaging and cell fluorescence imaging.

Besides, aptamers are short single-stranded DNA or RNA oligonucleotides that can specifically and selectively bind to small molecular ligands or protein targets with high affinity. Moreover, aptamers are highly specific, relatively small in size, non-immunogenic and can be readily stabilized by chemical modifications to enable the expansion of their diagnostic and therapeutic ability.<sup>28</sup> Till date, aptamers have been used as therapeutic aptamers for macular degeneration, oncology, diabetes, inflammation and coagulation. Among these aptamers, AS1411, a 26-base guanine-rich oligonucleotide (GRO) with an unmodified (phosphodiester) DNA backbone, is the first aptamer in clinical trials for the treatment of human cancer. The AS1411 aptamer could recognize nucleolin and be internalized in a variety of cancer cells, such as renal, breast and other adenocarcinoma cell lines.<sup>29</sup> In this study, the AS1411 aptamer was used to

improve the targeting ability of Mn-MoS<sub>2</sub> QDs to renal cell carcinoma.

Herein, in this study, we propose a novel Mn-doped MoS<sub>2</sub> QDs (Mn-MoS<sub>2</sub> QDs) via a “bottom-up” one-step hydrothermal technique for MR imaging and cell fluorescence labelling of renal cell carcinoma. AS1411 aptamer was used to improve the targeting ability of Mn-MoS<sub>2</sub> QDs to renal cell carcinoma.<sup>30</sup> The composition and structure of Mn-MoS<sub>2</sub> QDs were investigated by transmission electronic microscopy (TEM), atomic force microscope (AFM) and X-ray photoelectron spectrometer (XPS). The optical properties were analyzed with the photoluminescence (PL) emission spectra. We investigated the potential of application in cell fluorescence imaging using the Mn-MoS<sub>2</sub> QDs. Enhanced contrast effect of imaging was assessed by the in vitro MR cancer cell imaging and in vivo MR imaging with AS1411-Mn-MoS<sub>2</sub> QDs incubation. Finally, the long-term toxicity of Mn-MoS<sub>2</sub> QDs was investigated by the hematology and histological analysis. Therefore, the AS1411-Mn-MoS<sub>2</sub> QDs would be a potential candidate in dual-modal imaging for renal cell carcinoma diagnosis.

## Materials and Methods

### Materials

Glutathione and manganese nitrate tetrahydrate were purchased from Aladdin Chemical Reagent Co., Ltd. (Shanghai, China). Manganese nitrate tetrahydrate was received from Guoyao Group Chemical Reagents Co., Ltd. (Shanghai, China). Trichloromethane was obtained from Bailingwei Technology Co., Ltd. (Beijing, China). Reagents for cell cultures including fetal bovine serum, trypsin and RPMI1640 were supplied by Gibco. Thermo Fisher Scientific Co., Ltd. (Shanghai, China). DNA oligos were obtained from Shanghai Sangon Biotechnology Co. Ltd. (Shanghai, China). All chemicals involved in this work were analytical-grade. All aqueous solutions were prepared with ultrapure water ( $\geq 18$  M $\Omega$ , Milli-Q, Millipore). The DNA sequence was listed as follows. HS-SH-AS1411: 5'-HS-SH-GGTGGTGGTGGTGGTGGTGGTGGTGG-3'.

### Synthesis of Mn-Doped Molybdenum Disulfide Quantum Dots (Mn-MoS<sub>2</sub> QDs)

In this study, Mn-MoS<sub>2</sub> QDs were synthesized via “bottom-up” one-step hydrothermal method. Briefly, Mn(NO<sub>3</sub>)<sub>2</sub>·4H<sub>2</sub>O (12.5 mg) was dispersed in deionized water (5 mL), followed by the addition of Na<sub>2</sub>MoO<sub>4</sub>·2H<sub>2</sub>O (25 mg) and GSH (634 mg). The mixture was ultrasonicated for 10 mins and then

sealed in a poly(tetrafluoroethylene) (Teflon) autoclave. The autoclave was heated to and maintained at 200°C for 36 h, then cooled to the room temperature naturally. Subsequently, the resultant solution was filtered through 0.22  $\mu$ m microporous membrane and dialyzed against water in a dialysis bag to remove the unreacted raw materials. The AS1411 aptamer conjugation was realized by adding HS-SH-AS1411 (20  $\mu$ L, 250  $\mu$ mol/L) dropwise in Mn-MoS<sub>2</sub> QDs, then reacted in 37°C water bath for 2 hrs. Finally, the Mn-MoS<sub>2</sub> QDs and AS1411-Mn-MoS<sub>2</sub> QDs were obtained and stored under 4°C for further use.

### Characterization of Mn-MoS<sub>2</sub> QDs

The size, morphology and composition of Mn-MoS<sub>2</sub> QDs and AS1411-Mn-MoS<sub>2</sub> QDs were analyzed with a dynamic light scattering (DLS) analyzer (Zetasizer Nano ZS90, England), an atomic force microscope (AFM, SPI3800, Japan) and a high-resolution transmission electron microscopic (HR-TEM, JEOL JEM200CX, Japan) with energy dispersive X-ray function (EDS). X-ray photoelectron spectrometry (XPS) spectra were obtained from X-ray photoelectron spectrometer (XPS, Thermo escalab250Xi, USA). The content of Mn in Mn-MoS<sub>2</sub> QDs was assessed by an inductively coupled plasma mass spectrometry (ICP-MS, Optima 5300DV, PerkinElmer, USA). The UV-vis absorption spectra and PL emission of Mn-MoS<sub>2</sub> QDs were measured by a UV-vis NIR spectrometer (UH4150 HITACH) and LS55 Fluorescence Spectrometer (PerkinElmer, America), respectively. The absorbance for MTT assay was determined by a microplate reader (Multiskon MK3, USA) at 490 nm.

### In vitro Cell Cytotoxicity

#### Cell Culture

786-O renal carcinoma cells, MDA-MB-231 breast cancer cell, HO-8910 ovarian cancer stem cells, HK-2 renal tubular epithelial cells and EA.hy926 human umbilical vein endothelial cells were purchased from the Cell Bank of the Chinese Academy of Sciences (Shanghai, China). The aforementioned cell lines were maintained in RPMI medium containing 10% (v/v) FBS and penicillin–streptomycin (100  $\mu$ g/mL) and incubated at 37°C in a humidified 5% CO<sub>2</sub> atmosphere.

#### Cell Cytotoxicity Test

Cell cytotoxicity of Mn-MoS<sub>2</sub> QDs was determined via MTT method.<sup>31</sup> Briefly, the above-mentioned cells were seeded in 96-well plates for 24 hrs for cell attachment. Subsequently, Mn-MoS<sub>2</sub> QDs at various concentrations

were added in each cell and co-incubated for another 24 hrs. Then, 10  $\mu\text{L}$  MTT solution (5mg/mL) was added to each well with further incubation for 4 hrs. Afterwards, the MTT solution was removed and replaced with 100  $\mu\text{L}$  DMSO to dissolve the formazan crystals. Finally, the absorbance was detected at 490 nm using a BioTek Epoch microplate reader (Multiskon MK3, USA).

## Bioimaging and Cell Labelling

The 786-O and EA.hy926 cells were used to assess the ability of Mn-MoS<sub>2</sub> QDs as fluorescence cell labelling agent. Cells were seeded on sterile coverslips in a 6-well plate overnight for cell attachment. Then, the cells were incubated with Mn-MoS<sub>2</sub> QDs (2 mM) or AS1411-Mn-MoS<sub>2</sub> QDs (2 mM) for 2 hrs for cellular labelling. Subsequently, the cells were washed three times with PBS. Finally, the samples were observed using a fluorescence microscopy.

## T<sub>1</sub> Relaxivity of Mn-MoS<sub>2</sub> QDs

The T<sub>1</sub>-weighted MRI contrast measurement of Mn-MoS<sub>2</sub> QDs was conducted on a 3.0T Discovery 750W MR system. Mn-MoS<sub>2</sub> QDs were analyzed over various Mn concentrations of 0.345, 0.689, 1.379, 2.758, 5.516, 11.03 and 22.06 mM. The T<sub>1</sub>-weighted MR images of these samples were obtained with Spin-Echo sequence under the following parameters: TR= 425ms, TE=Min Full, matrix size =384×224, field of view=18 cm×18 cm, slice thickness=3.0 mm, spacing= 1.5 mm.

## In vitro Enhanced MR Imaging

To assess the MR cellular imaging ability of Mn-MoS<sub>2</sub> QDs and AS1411-Mn-MoS<sub>2</sub> QDs, 786-O and EA.hy926 cells were inoculated on 6-well plates overnight at a density of  $2 \times 10^5$  cells/well. Subsequently, the cells were co-incubated with Mn-MoS<sub>2</sub> QDs or AS1411-Mn-MoS<sub>2</sub> QDs at a concentration of 2 mM for 2 hrs to allow cellular uptake. Thereafter, the cells were washed thrice with cold PBS and trypsinized with EDTA-trypsin, then were resuspended in 300  $\mu\text{L}$  1% agarose gel. Finally, the MR imaging was conducted on the previous MR system.

## In vivo MR Imaging

For in vivo MRI, the tests were investigated on 786-O bearing BALB/c nude mice (male, 5 weeks old) and approved by the Animal Care Committee of Xuzhou Medical University, and were performed in accordance with the committee's guidelines. To develop the 786-O bearing mice, cells ( $2 \times 10^6$ ) suspended in serum-free cell

medium were subcutaneously injected on the back of each nude mouse. When the tumor volume reached about 1 cm<sup>3</sup>, the mice were injected with Mn-MoS<sub>2</sub> QDs or AS1411-Mn-MoS<sub>2</sub> QDs (200  $\mu\text{L}$  2mM Mn) for in vivo imaging. The MRI studies were performed on the previous MR system pre- and post-injection (0.25, 0.5, 0.75, 1, 2, 3, 4, 6, 12 hrs).

## In vivo Toxicity Analysis

In vivo toxicity test was performed on the healthy Kunming mice (female, 8 weeks). The animals were randomly divided into two groups: Control and AS1411-Mn-MoS<sub>2</sub> QDs (200  $\mu\text{L}$  2mM Mn), each group containing six mice. The blood samples were collected on days 1, 7 and 21 for blood serum analysis. Then, the blood samples were centrifuged at 3000 rpm for 5 mins to obtain the serum for biochemistry analysis.<sup>32</sup> Simultaneously, the mice were sacrificed to harvest the major organs (heart, liver, spleen, kidney and lung). Afterwards, the organs were fixed with 10% formalin, sectioned and stained with hematoxylin and eosin (H&E). Finally, the histological samples were examined under an optical microscope.

## Statistical Analysis

SPSS 16.0 software (Chicago, IL) was used for statistical analysis. One-way ANOVA and Dunnett *t*-tests were used to compare the statistical significance between different groups. Quantitative data are presented as mean  $\pm$  SD,  $p < 0.05$  was considered significant in all cases.

## Results and Discussion

### Synthesis and Characterization of Mn-MoS<sub>2</sub> QDs

In this study, Mn-MoS<sub>2</sub> QDs were synthesized via “bottom-up” one-step hydrothermal method using manganese nitrate tetrahydrate, sodium molybdate, and glutathione as manganese, molybdenum and sulfur sources, respectively. As shown in Figure 1A, a typical spherical morphology was observed in the TEM image of Mn-MoS<sub>2</sub> QDs. Mn-MoS<sub>2</sub> QDs exhibited excellent crystal structure with noticeable lattice fringes (spacing=0.24 nm) showed in the high-resolved TEM images (inset in Figure 1A). The spacing was consistent with the typical lattice of the MoS<sub>2</sub> QDs, indicating that the doping of Mn induced no obvious change to the crystal structure of MoS<sub>2</sub> QDs.<sup>21,22,24</sup> Moreover, the Mn-MoS<sub>2</sub> QDs were well dispersed with a narrow size distribution and an average diameter of approximately 6.07 nm (Figure 1B). The content of Mn in Mn-MoS<sub>2</sub>

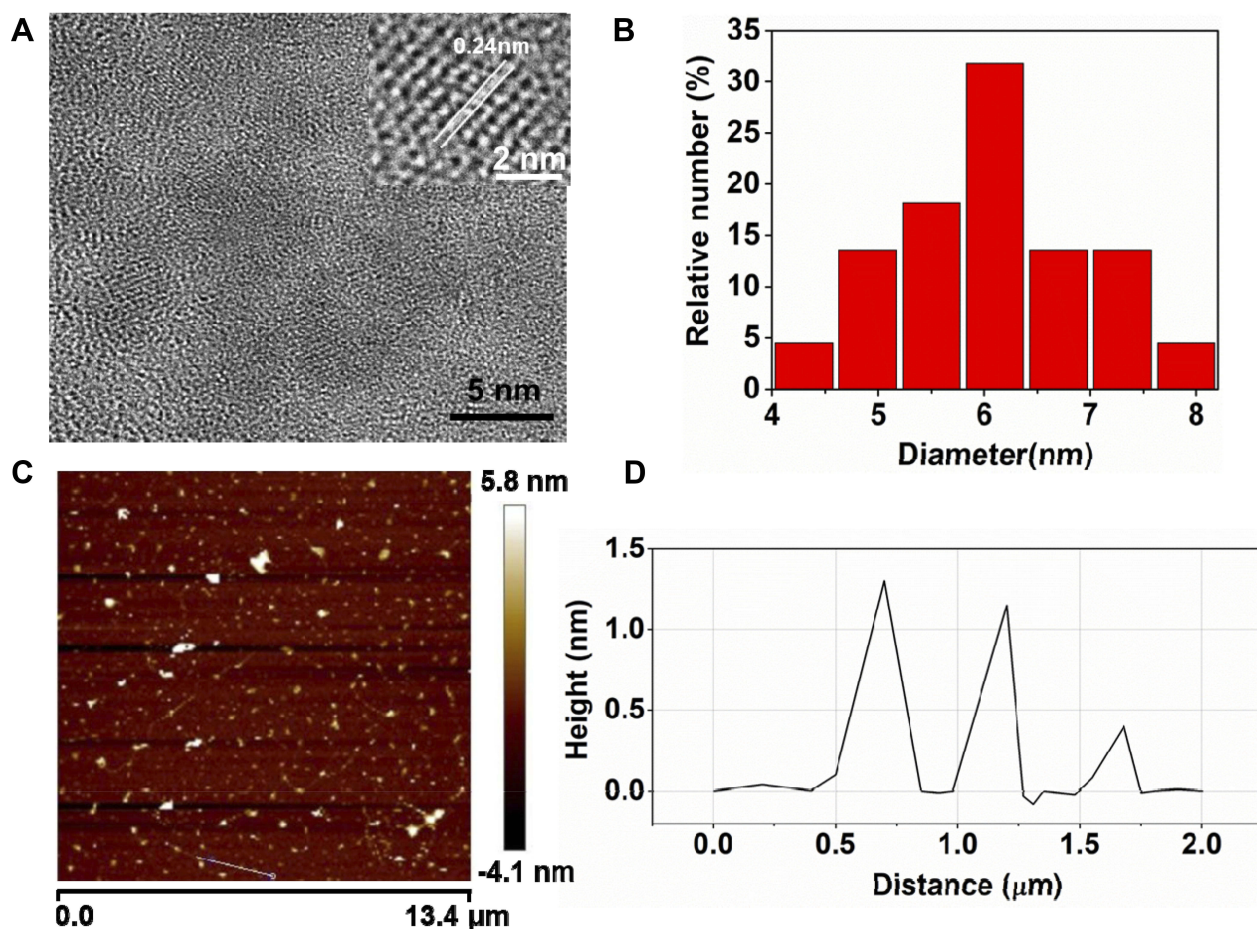


**Figure 1** Characterizations of Mn-MoS<sub>2</sub> QDs: (A) TEM images of Mn-MoS<sub>2</sub> QDs (inset, high-resolution TEM images), (B) size distributions of Mn-MoS<sub>2</sub> QDs, (C) AFM image of Mn-MoS<sub>2</sub> QDs, and (D) size and height distributions of the MoS<sub>2</sub> QDs.

QDs was further assessed by ICP-MS, and was calculated to be 9.5 (wt %), which is sufficient for the T<sub>1</sub>-weighted MR imaging. Furthermore, AFM was conducted to investigate the thickness and morphology of Mn-MoS<sub>2</sub> QDs. As shown in the AFM image (Figure 1C and D), the thickness ranged from 0.6 to 1.2 nm, indicating the monolayer or bilayer structure of the as-prepared Mn-MoS<sub>2</sub> QDs.<sup>24</sup>

The XPS analysis was also conducted to evaluate the chemical structure of Mn-MoS<sub>2</sub> QDs. As shown in high-resolution Mo 3d spectrum in Figure 2B, two typical peaks were observed at 228.1 eV and 232.6 eV, which corresponded to the Mo 3d<sub>3/2</sub> and Mo 3d<sub>5/2</sub>, respectively, indicating that the Mo element existed as 4+ oxidation state in Mn-MoS<sub>2</sub> QDs. The peaks at 163.4 eV and 169.7 eV belong to the S 2p<sub>3/2</sub> and S 2p<sub>1/2</sub> orbitals of divalent sulfide ions (Figure 2C). Furthermore, two characteristic peaks were observed at 640.8 eV and 642.4 eV, which correspond to the spin-orbit coupled Mn 2p<sub>3/2</sub>, suggesting that the valence state of Mn-MoS<sub>2</sub> QDs was divalent and

tetravalent (Figure 2A). These results demonstrated the successful synthesis of Mn-MoS<sub>2</sub> QDs.

### Optical Features of Mn-MoS<sub>2</sub> QDs

The optical property of the Mn-MoS<sub>2</sub> QDs was characterized by ultraviolet-visible spectroscopy (UV-vis). As shown in Figure 3A, the UV-vis spectra of Mn-MoS<sub>2</sub> QDs showed a shoulder peak located at 290 nm attributed to the blue-shifted excitonic peaks. Typically, the excitonic peaks always blue shift with the formation of MoS<sub>2</sub> QDs. The UV-vis spectra result further confirmed the successful formation of Mn-MoS<sub>2</sub> QDs. The fluorescence spectra of the Mn-MoS<sub>2</sub> QDs were measured at various excitation wavelengths from 260 to 380 nm and shown in Figure 3C and D. The excitation at 290 nm induced a strong luminescence band with a maximum at 380 nm (Figure 3B). And the emission peak red-shifted from 380 to 435 nm within the excitation wavelength ranging from 260 to 380 nm. The excitation-dependent emission is consistent with the previous studies. The

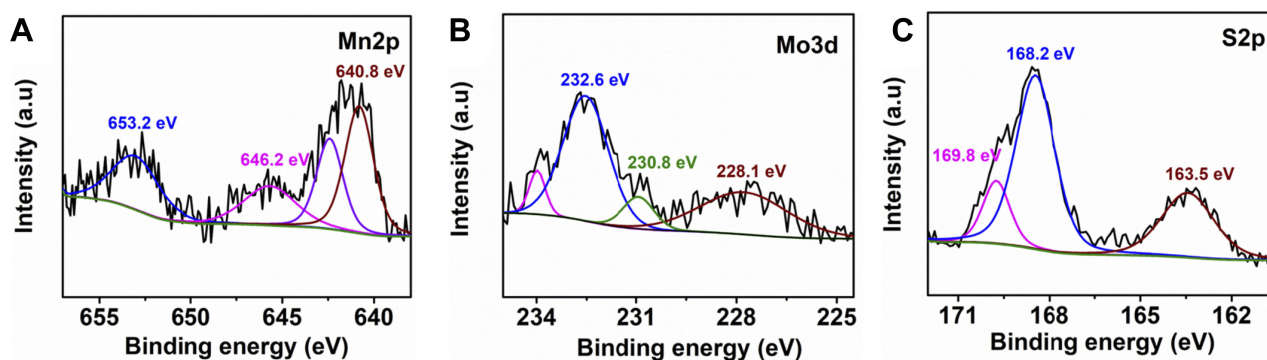


Figure 2 XPS spectra of the Mn-MoS<sub>2</sub> QDs: (A) Mn2p, (B) Mo3d, and (C) S2p.

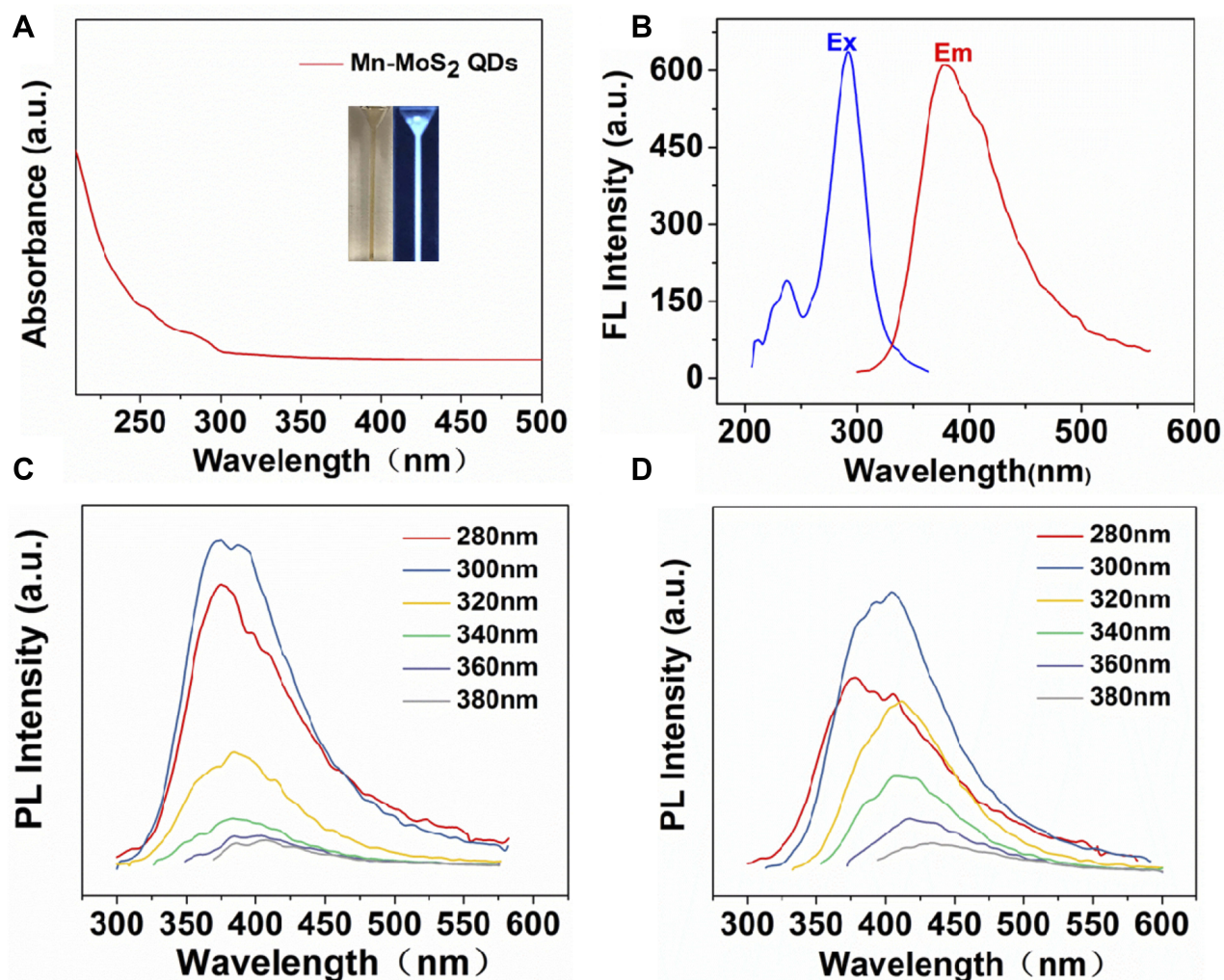


Figure 3 Optical properties of Mn-MoS<sub>2</sub> QDs: (A) UV-vis absorption spectra of Mn-MoS<sub>2</sub> QDs, (B) PL emission and excitation of the Mn-MoS<sub>2</sub> QDs, (C) fluorescence emission spectra of the Mn-MoS<sub>2</sub> QDs at different excitation wavelengths, and (D) fluorescence emission spectra of the Mn-MoS<sub>2</sub> QDs at different excitation wavelengths.

Mn-MoS<sub>2</sub> QDs aqueous were observed as pale pink under natural light, but revealed vivid blue luminescence under the UV light excitation (Figure 3A inset). Furthermore, the

quantum yield (QY) of Mn-MoS<sub>2</sub> QDs was assessed by comparing with the quinine sulfate standard, and was calculated to be 41.45% (Figure S1). The QY value was much

higher than that of MoS<sub>2</sub> nanosheets and other quantum dots. The excellent luminescence and high QY of the Mn-MoS<sub>2</sub> QDs enabled their potential application in cell labelling.

## T<sub>1</sub> Relaxivity

To evaluate the possibility of using Mn-MoS<sub>2</sub> QDs as MRI contrast agents, the T<sub>1</sub> relaxation times of the QDs at various Mn concentrations were measured with a 3.0T MR system. The T<sub>1</sub> relaxation time decrease with the increase of the amounts of Mn-MoS<sub>2</sub> QDs. As shown in Figure 5B, Mn-MoS<sub>2</sub> QDs clearly exhibited bright signal enhancement in the T<sub>1</sub>-weighted MR imaging. Furthermore, the bright signal enhancement indicated a concentration-dependent relation with the prepared Mn-MoS<sub>2</sub> QDs, thus manifesting their potential application as a T<sub>1</sub>-weighted contrast agent (Figure 5A). The longitudinal relaxation rate (1/T<sub>1</sub>), also known as relaxivity r<sub>1</sub>, was calculated to be 16.95 mM<sup>-1</sup>s<sup>-1</sup>, which was 4-fold of the commercial product Gd-DTPA (4.21 mM<sup>-1</sup>s<sup>-1</sup>, Figure S2). The high r<sub>1</sub> relaxivity value of Mn-MoS<sub>2</sub> QDs might be mainly ascribed to high concentration of metal ions exposed on the surface of nanoparticles which favored the longitudinal relaxation of the water proton to present a better contrast effect. Furthermore, as shown in Figure S3, AS1411 conjugation did not induce significant change on the MRI contrast effect of Mn-MoS<sub>2</sub> QDs. These results indicated that the prepared Mn-MoS<sub>2</sub> QDs could be a potential contrast agent for MR imaging to enhance the relaxivity of the commercial Gd-DTPA.

## In vitro Cytotoxicity of Mn-MoS<sub>2</sub> QDs

Although the prepared Mn-MoS<sub>2</sub> QDs exhibited excellent MR contrast and PL property in aqueous solution, it is of great significance to ensure good biocompatibility of the QDs to be applied in cell labelling and tracking in the biological system. At first, the cytotoxicity of Mn-MoS<sub>2</sub> QDs at various concentrations was assessed against 786-O renal carcinoma and EA.hy926 normal umbilical vein endothelial cells. As shown in Figure 4A, the viability of EA.hy926 normal umbilical vein endothelial cells remained above 85% following with the incubation of Mn-MoS<sub>2</sub> QDs even at a high concentration of 0.22 mM. In contrast, the Mn-MoS<sub>2</sub> QDs indicated obvious toxicity to the 786-O cancer cells under the same situation. To further investigate the different appearance between normal and cancer cells, Mn-MoS<sub>2</sub> QDs were co-incubated with MDA-MB-231 breast cancer, HO-8910 ovarian cancer and HK-2 renal tubular cells. As indicated in Figure 4B, similarly, Mn-MoS<sub>2</sub> QDs revealed low toxicity to HK-2 normal cells and concentration-dependent cytotoxicity to the MDA-MB-231 breast cancer and HO-8910 ovarian cancer cells. Normally, the tumor microenvironment and lysosome exhibited mildly acidic and H<sub>2</sub>O<sub>2</sub>-rich property compared with the normal tissues. As reported, the Mn contained QDs indicated noticeable anticancer effect by the production of oxygen with H<sub>2</sub>O<sub>2</sub> triggered by Mn contained QDs.<sup>33</sup> Therefore, in this study, the cancer cytotoxicity associated with Mn-MoS<sub>2</sub> QDs may also be attributed to the generation of singlet oxygen from H<sub>2</sub>O<sub>2</sub>

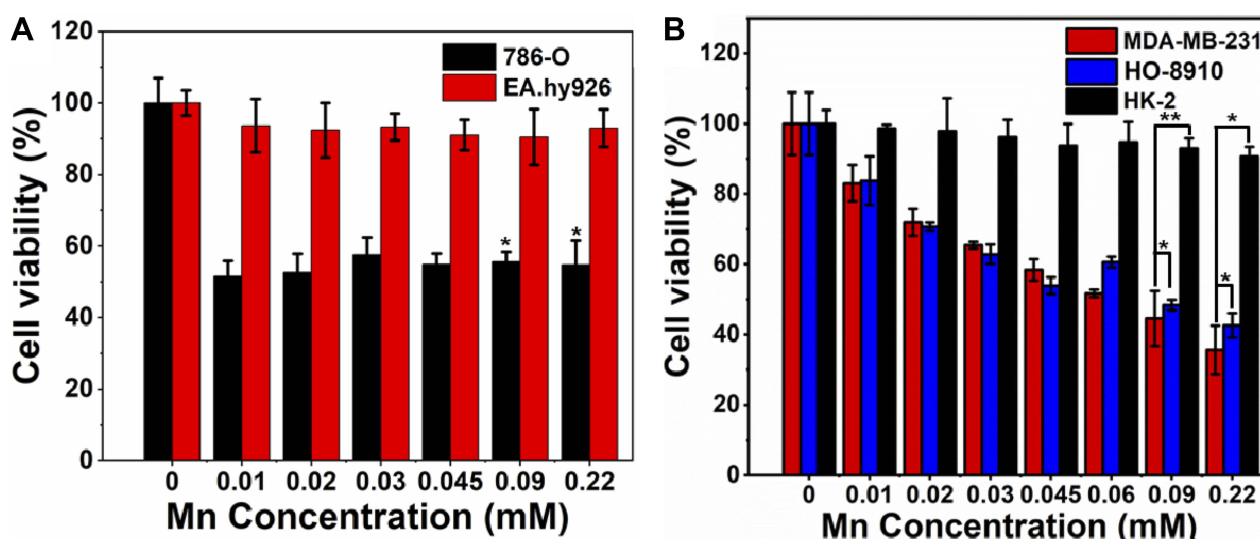


**Figure 4** In vitro cytotoxicity test of Mn-MoS<sub>2</sub> QDs against (A) 786-O and EA.hy926 cells, \**p* < 0.05 was compared to EA.hy926 cell of the same treated concentrations and (B) MDA-MB-231, HO-8910 and HK-2 cells, \**p* < 0.05 and \*\**p* < 0.01.

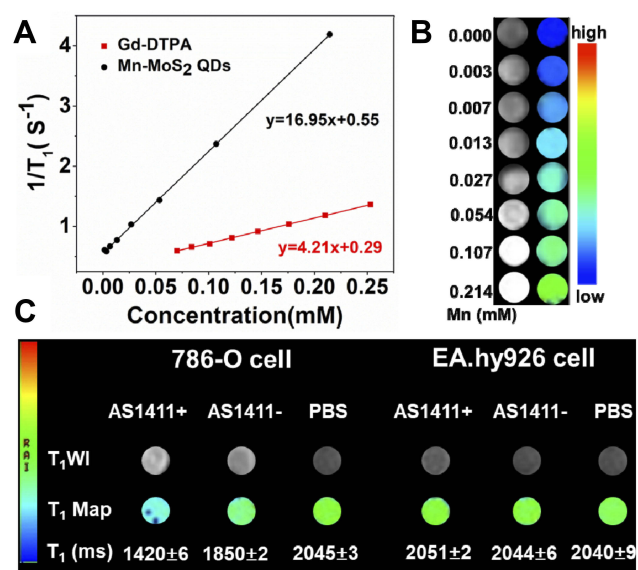


**Figure 5** MR contrast ability of Mn-MoS<sub>2</sub> QDs: (A) linear relationship between longitudinal relaxation rate of Mn-MoS<sub>2</sub> QDs and Gd-DTPA at different concentrations, (B) T<sub>1</sub>-weighted phantom images of Mn-MoS<sub>2</sub> QDs at different Mn concentrations using a 3.0T MR scanner, (C) T<sub>1</sub>-weighted 786-O and EA.hy926 cellular MR imaging with Mn-MoS<sub>2</sub> QDs and AS1411-Mn-MoS<sub>2</sub> QDs.

decomposition in the tumor microenvironment and lysosome. These results demonstrated that Mn-MoS<sub>2</sub> QDs represented wonderful biocompatibility to the normal cells and killing-effect to various cancer cells.

## In vitro Cell Labelling

Encouraged by the excellent PL property of the as-prepared Mn-MoS<sub>2</sub> QDs, we moved to investigate the cell labelling ability of QDs on 786-O and EA.hy926 cells. AS1411 aptamer was used to conjugate on the Mn-MoS<sub>2</sub> QDs to improve the affinity of the QDs to the 786-O cells. As shown in Figure 6, no obvious fluorescence was observed in EA.hy926 cells under the incubation with Mn-MoS<sub>2</sub> QDs and AS-1411-Mn-MoS<sub>2</sub> QDs. In comparison, the 786-O cells displayed weak blue fluorescence after the

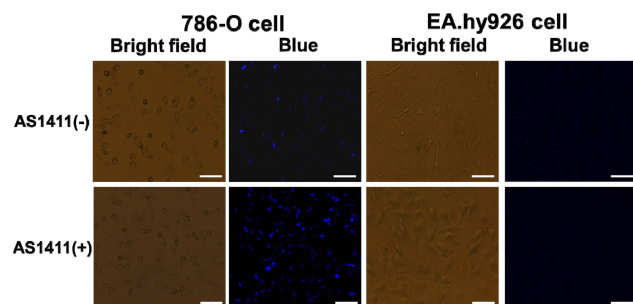


**Figure 6** Fluorescence imaging of 786-O cells and EA.hy926 cells labeled with Mn-MoS<sub>2</sub> QDs and AS1411-Mn-MoS<sub>2</sub> QDs, scale bar = 50μm.

staining with Mn-MoS<sub>2</sub> QDs. However, after the AS1411 conjugation, the blue fluorescence was significantly improved in the 786-O cells after staining. It indicated that the AS1411 aptamer could improve the binding of Mn-MoS<sub>2</sub> QDs with 786-O cells. Cell surface nucleolin is selectively expressed in cancer cells compared to normal cells, and that it mediates the binding and uptake of AS1411 in cancer cells.<sup>34</sup> The 786-O renal carcinoma cells also reported high expression of nucleolin on the outer surface of cell membrane.<sup>35</sup> Therefore, the AS1411 aptamer modified Mn-MoS<sub>2</sub> QDs could specifically bind to nucleolin on the surface of 786-O renal carcinoma cells and taken up by the cells through the macropinocytosis process. It demonstrated that the AS1411-Mn-MoS<sub>2</sub> QDs could serve as promising and specific fluorescent probe for the labelling of 786-O renal carcinoma cells.

## In vitro Specific MR Imaging

The specific cellular targeting of the QDs was further investigated by the T<sub>1</sub>-weighted MR imaging of 786-O and EA.hy926 cells. The cells were co-incubated with PBS buffer, Mn-MoS<sub>2</sub> QDs and AS1411-Mn-MoS<sub>2</sub> QDs, respectively. As shown in the T<sub>1</sub>-weighted MR images and T<sub>1</sub>-mapping images (Figure 5C), the Mn-MoS<sub>2</sub> QDs did not induce obvious MR enhancement to the EA.hy926 cells compared with the PBS treated group. In addition, AS1411 conjugation did not lead to significant effect on the MRI behavior ascribed to the low expression of nucleolin on the normal cells (Figure 5C). However, the 786-O cells exhibited brighter signal after the incubation of Mn-MoS<sub>2</sub> QDs compared with the EA.hy926 cells, indicating the higher cellular uptake of Mn-MoS<sub>2</sub> QDs by cancer cells. Furthermore, the T<sub>1</sub> signal was significantly enhanced for 786-O cells in the presence of AS1411 aptamer. It demonstrated that the AS1411 aptamer could facilitate the QDs to bind with the nucleolin on the surface of cancer cells to result in a higher T<sub>1</sub> signal. These results demonstrated that the 786-O cancer cells could be specifically marked by the AS1411-Mn-MoS<sub>2</sub> QDs with fluorescence/MR dual-modal imaging mode.

## In vivo MRI

The potential of AS1411-Mn-MoS<sub>2</sub> QDs as a MRI contrast agent for in vivo cancer imaging was investigated using BALB/c nude mice with 786-O renal carcinoma. T<sub>1</sub>-weighted MRI scans were conducted prior to, and at various time points post-injection of Mn-MoS<sub>2</sub> QDs and AS1411-Mn-MoS<sub>2</sub> QDs. As shown in Figure 7A and B, compared with the pre-injected mice, the tumor exhibited contrast-enhanced regions 15-min post-injection following

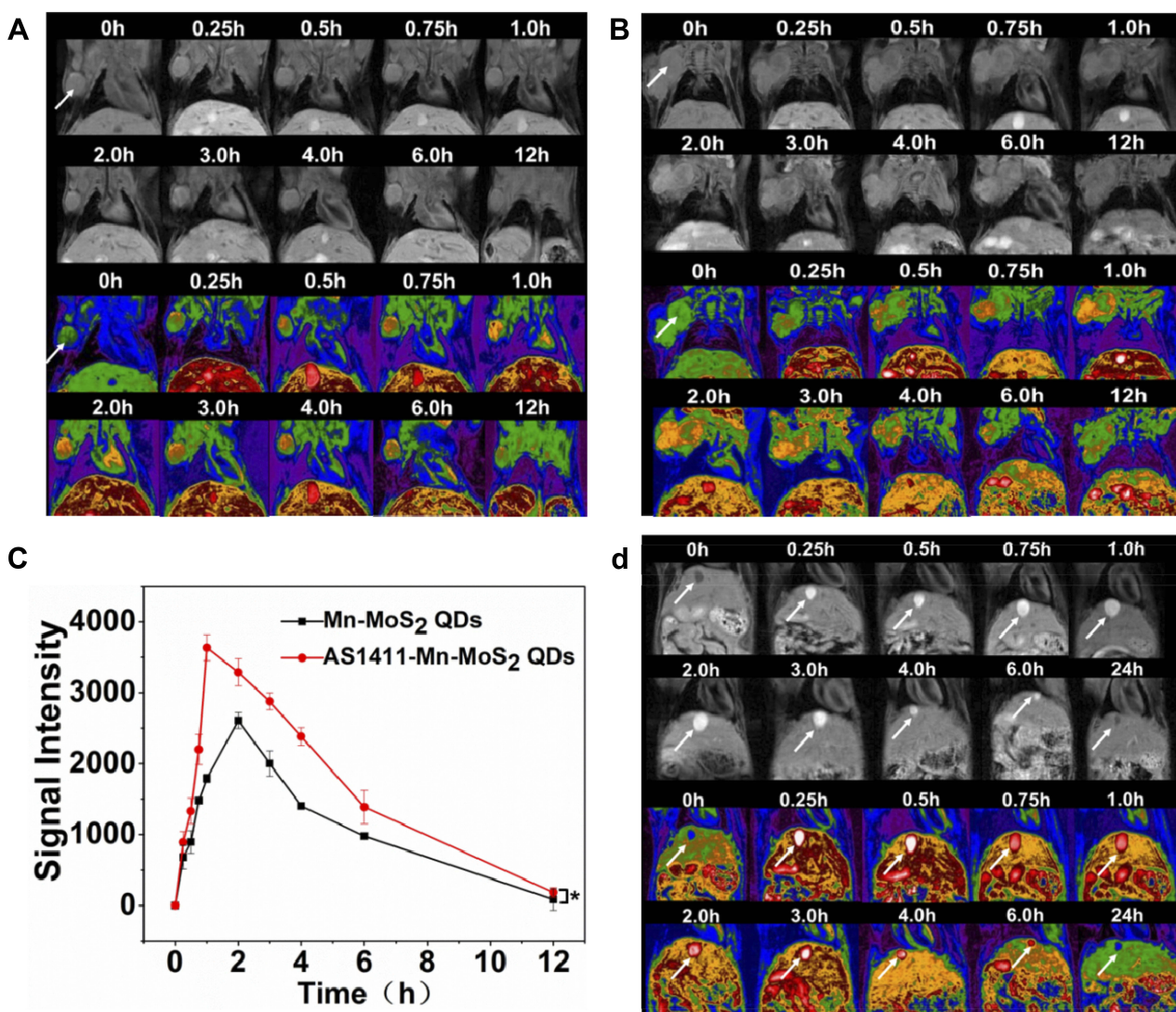


**Figure 7** T<sub>1</sub>-weighted in vivo MR imaging of mice pre- and post-injection of (A) Mn-MoS<sub>2</sub> QDs and (B) AS1411-Mn-MoS<sub>2</sub> QDs nanoprobe at different time points, the white arrows indicate tumor, \**p* < 0.05. (C) Signal intensity in the tumors, (D) T<sub>1</sub>-weighted MR images of mice pre- and post-injection of Mn-MoS<sub>2</sub> QDs. The white arrows indicate gall bladder.

the accumulation of Mn-MoS<sub>2</sub> QDs and AS1411-Mn-MoS<sub>2</sub> QDs. The T<sub>1</sub> MR signal gradually became brighter within 1–2 hrs, then turned weaker following the time. Particularly, the AS1411-Mn-MoS<sub>2</sub> QDs showed much brighter signal in T<sub>1</sub>-weighted images at the same time point in the tumor regions compared with the Mn-MoS<sub>2</sub> QDs, indicating that the AS1411 aptamer could improve the accumulation of Mn-MoS<sub>2</sub> QDs in the tumor tissues, thus enhancing the MR contrast effect. The measured MR intensity values of the tumors were presented in Figure 7C. The MR signal intensity values of AS1411-Mn-MoS<sub>2</sub> QDs were higher than the counterparts in all time points, which was consistent with the T<sub>1</sub>-mapping MR images. It further demonstrated the targeting ability of the QDs to the tumor

benefit from the AS1411 aptamer. In addition, as shown in Figure 7D, high MR signal was also observed within 6 hrs post-injection in the gall bladder and liver. However, the signal in the liver and bladder became weaker, indicating that the clearance of the QDs was mainly completed by hepatobiliary system. Overall, the in vivo MRI suggested the potential applications of AS1411-Mn-MoS<sub>2</sub> QDs for renal carcinoma diagnosis.

### In vivo Cytotoxicity of Mn-MoS<sub>2</sub> QDs

In vivo cytotoxicity studies of the Mn-MoS<sub>2</sub> QDs were investigated on the healthy Kunming mice for 21 days. The Mn-MoS<sub>2</sub> QDs were suspended in PBS and injected in the mice via tail vein with the saline injected mice as

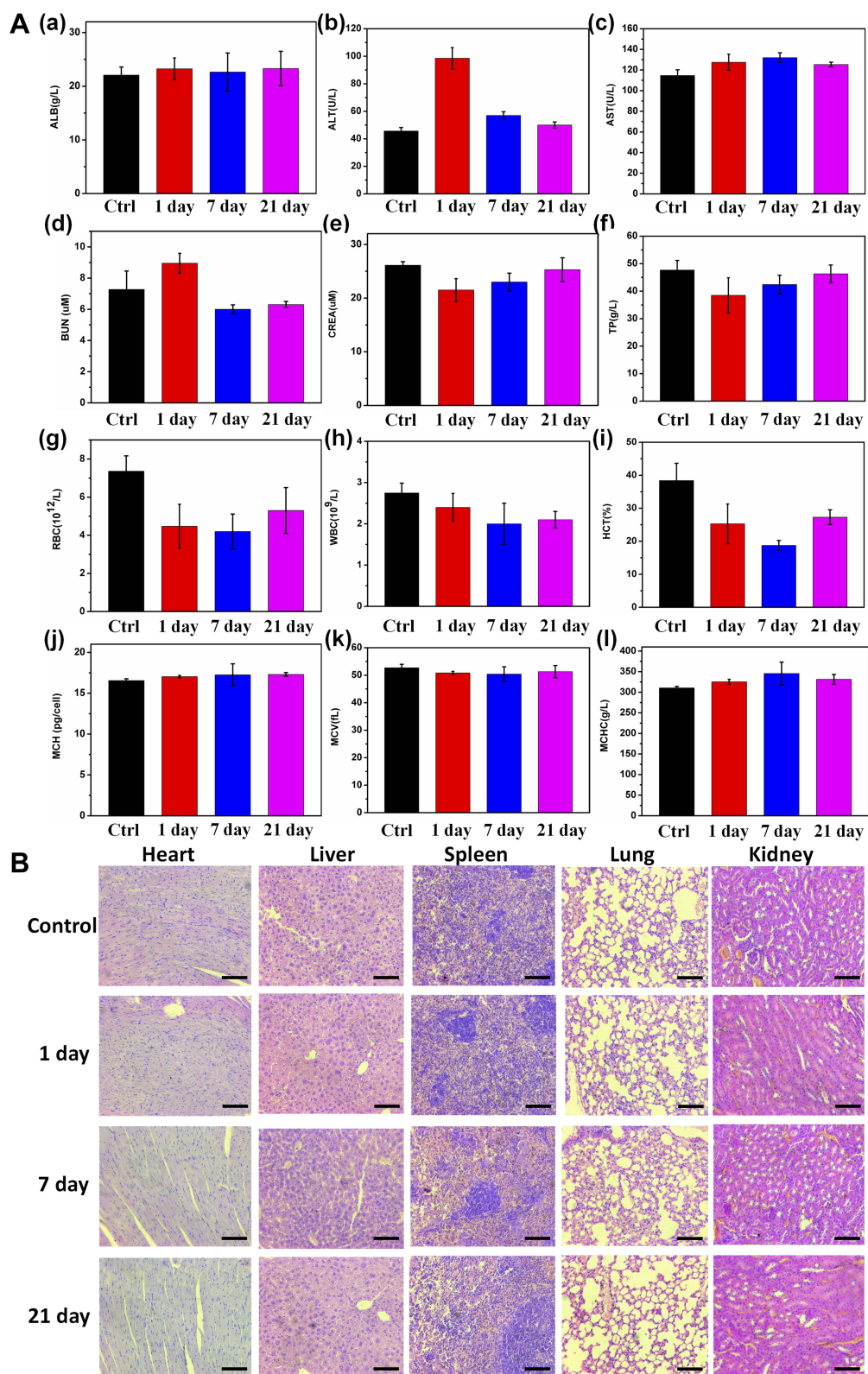


**Figure 8** In vivo toxicity test of Mn-MoS<sub>2</sub> QDs: **(Aa–l)** Mouse serum biochemistry analysis and blood routine analysis before (0d, control) and after injection of Mn-MoS<sub>2</sub> QDs for 1, 7, 21d. **(B)** Histological images of the heart, lungs, liver, spleen and kidneys of mice 1, 7 and 21 days post-intravenous injection of Mn-MoS<sub>2</sub> QDs and in control mice. The organs were sectioned and stained with hematoxylin and eosin (H&E) and observed under a light microscope, scale bar = 100 μm.

control. Blood was collected after 1, 7, 21 days administration and investigated with complete blood count and serum biochemistry analysis. For the hematology study, we selected several important indicators as white blood cells (WBC), red blood cells (RBC), hematocrit (HCT), mean corpuscular volume (MCV), mean corpuscular hemoglobin (MCH) and mean corpuscular hemoglobin concentration (MCHC). As shown in Figure 8A, the hematological factors did not exhibit obvious difference between the control and Mn-MoS<sub>2</sub> QDs injected groups. Only the WBC and RBC values showed slight decrease in the Mn-MoS<sub>2</sub> QDs injected mice compared with the control. However, all the hematological values including WBC still maintained within the normal range, indicating no acute toxicity. Serum biochemistry analysis was also performed to assess the potential toxicity of the Mn-MoS<sub>2</sub> QDs on mice.<sup>33</sup> As shown in Figure 8A, the blood urea nitrogen (BUN) maintained normal level, indicating the good condition of the kidney. Otherwise, the damage to the renal function may induce the increase of urea nitrogen in the blood. Furthermore, the hepatic function markers – albumin (ALB), alanine aminotransferase (ALT), aspartate aminotransferase (AST) and total protein (TP) revealed a slight discrepancy in 1 day, but returned to the normal level in 7 and 21 days. However, all the hepatic indicators maintained within the normal ranges, demonstrating that Mn-MoS<sub>2</sub> QDs may affect the hepatic function in the short time after administration but without liver injury in a long term.

Histological analysis for the major organs (heart, liver spleen, lung, kidney) was also performed to identify the effect of Mn-MoS<sub>2</sub> QDs to various tissues. As shown in Figure 8B, there was no obvious inflammation or damage lesions observed in major organs after 21-day injection of Mn-MoS<sub>2</sub> QDs. The H&E images exhibited similar morphology in the different organs compared with the control groups. These results suggested the low toxicity of the Mn-MoS<sub>2</sub> QDs in the animal body, unlocking their potential in biomedical applications.

## Conclusions

A novel AS1411-Mn-MoS<sub>2</sub> nanoprobe was successfully synthesized via bottom-up one-step hydrothermal technique for targeted MR and fluorescence imaging of renal clear cell carcinoma. The as-prepared AS1411-Mn-MoS<sub>2</sub> QDs exhibited excellent aqueous property, intense luminescence, low toxicity and high quantum yield. Owing to the strong absorption and emission in the visible region,

AS1411-Mn-MoS<sub>2</sub> QDs were successfully applied in cell labelling for renal cell carcinoma. Besides, AS1411-Mn-MoS<sub>2</sub> QDs also revealed wonderful targeted MR contrast behavior for the renal carcinoma in the in vitro and in vivo MR tests compared with the clinical Gd-DTPA. Therefore, the experimental results demonstrate that the AS1411-Mn-MoS<sub>2</sub> QDs could be used as a nanoprobe for the specific recognition of renal clear cell carcinoma.

## Acknowledgment

This work was supported by the National Natural Science Foundation of China (81771904, 81901798), Natural Science Foundation of Jiangsu Province for the Excellent Young Scholars (BK20170054), Natural Science Fund for Colleges and Universities in Jiangsu Province (19KJB310025), Startup Fund for Youth Talent in Xuzhou Medical University (D2019028), China Postdoctoral Science Foundation (2016M601890, 177607), Qing Lan Project, the Peak of Six Talents of Jiangsu Province (WSN-112), Jiangsu Provincial Medical Youth Talent (QNRC2016776), Six One Project of Jiangsu Province (LGY2018083), and the Science and Technology Development Program of Xuzhou (KC19141).

## Disclosure

There are no conflicts of interest.

## References

1. Bray F, Ferlay J, Soerjomataram I, Siegel RL, Torre LA, Jemal A. Global cancer statistics 2018: GLOBOCAN estimates of incidence and mortality worldwide for 36 cancers in 185 countries. *CA Cancer J Clin*. 2018;68(6):394–424. doi:10.3322/caac.21492
2. Wong MCS, Goggins WB, Yip BHK, et al. Incidence and mortality of kidney cancer: temporal patterns and global trends in 39 countries. *Sci Rep*. 2017;7:15698. doi:10.1038/s41598-017-15922-4
3. Hsieh JJ, Purdue MP, Signoretti S, et al. Renal cell carcinoma. *Nature Rev Dis Primers*. 2017;9(3):17009. doi:10.1038/nrdp.2017.9
4. Lee DE, Koo H, Sun IC, Ryu JH, Kim K, Kwon IC. Multifunctional nanoparticles for multimodal imaging and theragnosis. *Chem Soc Rev*. 2012;41:2656–2672. doi:10.1039/C2CS15261D
5. Evertsson M, Kjillman P, Cinthio M, et al. Combined magnetomotive ultrasound, PET/CT and MR imaging of 68Ga-labelled superparamagnetic iron oxide nanoparticles in rat sentinel lymph nodes in vivo. *Sci Rep*. 2017;7:4824. doi:10.1038/s41598-017-04396-z
6. Yang W, Guo W, Le W, et al. Albumin-bioinspired Gd: CuS nanotheranostic agent for in vivo photoacoustic/magnetic resonance imaging-guided tumor-targeted photothermal therapy. *ACS Nano*. 2016;10:1024510257. doi:10.1021/acsnano.6b05760
7. Zhou R, Sun S, Li C, Wu L, Hou X, Wu P. Enriching Mn-doped ZnSe quantum dots onto mesoporous silica nanoparticles for enhanced fluorescence/magnetic resonance imaging dual-modal bio-imaging. *ACS Appl Mater Interfaces*. 2018;10:34060–34067. doi:10.1021/acsnano.8b14554
8. Hart AG, Bowtell RW, Kockenberger W, Wensellers T, Ratnieks FL. Magnetic resonance imaging in entomology: a critical review. *J Insect Sci*. 2003;3:5. doi:10.1673/031.003.0501

9. David K, Hildebrandt N. Quantum dots: bright and versatile in vitro and in vivo fluorescence imaging probes. *Chem Soc Rev*. 2015;44:4792–4834.
10. Yao YY, Gedda G, Girma WM, Yen CL, Ling YC, Chang JY. Magnetofluorescent carbon dots derived from crab shell for targeted dual-modality bioimaging and drug delivery. *ACS Appl Mater Interfaces*. 2017;9:13887–13899. doi:10.1021/acsami.7b01599
11. Liu Y, Zhang N. Gadolinium loaded nanoparticles in theranostic magnetic resonance imaging. *Biomaterials*. 2012;33(21):5363–5375. doi:10.1016/j.biomaterials.2012.03.084
12. Semelka RC, Ramalho M, Alobaidy M, Ramalho J. Gadolinium in humans: a family of disorders. *Am J Roentgenol*. 2016;207(2):229–233. doi:10.2214/AJR.15.15842
13. Pan D, Caruthers SD, Senpan A, Schmieder AH, Wickline SA, Lanza GM. Revisiting an old friend: manganese-based MRI contrast agents. *Wires Nanomed Nanobiotechnol*. 2011;3:162–173. doi:10.1002/wnan.116
14. Aggett PJ. I Physiology and metabolism of essential trace elements: an outline. *Clin Endocrinol Metab*. 1985;14(3):513–543. doi:10.1016/S0300-595X(85)80005-0
15. Pan D, Schmieder AH, Wickline SA, Lanza GM. Manganese-based MRI contrast agents: past, present and future. *Tetrahedron*. 2011;67:8431–8444. doi:10.1016/j.tet.2011.07.076
16. Michslet X, Pinaud FF, Bentolila LA, et al. Quantum dots for live cells, in vivo imaging, and diagnostics. *Science*. 2005;307(5709):538–544. doi:10.1126/science.1104274
17. Roy P, Periasamy AP, Lin CY, et al. Photoluminescent graphene quantum dots for in vivo imaging of apoptotic cells. *Nanoscale*. 2015;7:2504–2510. doi:10.1039/C4NR07005D
18. Zheng S, Yu N, Han C, et al. Preparation of gadolinium doped carbon dots for enhanced MR imaging and cell fluorescence labelling. *Biochem Biophys Res Commun*. 2019;511(2):207–213. doi:10.1016/j.bbrc.2019.01.098
19. Frasco MF, Chaniotakis N. Semiconductor quantum dots in chemical sensors and biosensors. *Sensors*. 2009;9(9):7266–7286. doi:10.3390/s90907266
20. Barua S, Dutta HS, Gogoi S, Devi R, Khan R. Nanostructured MoS<sub>2</sub>-based advanced biosensors: a review. *ACS Appl Nano Mater*. 2018;1(1):2–25. doi:10.1021/acsanm.7b00157
21. Zhou K, Zhang Y, Xia Z, Wei W. As-prepared MoS<sub>2</sub> quantum dot as a facile fluorescent probe for long-term tracing of live cells. *Nanotechnology*. 2016;27:275101. doi:10.1088/0957-4484/27/27/275101
22. Lin H, Wang C, Wu J, Xu Z, Huang Y, Zhang C. Colloidal synthesis of MoS<sub>2</sub> quantum dots: size-dependent tunable photoluminescence and bioimaging. *N J Chem*. 2015;39:8492–8497. doi:10.1039/C5NJ01698C
23. Wang Y, Ni Y. Molybdenum disulfide quantum dots as a photoluminescence sensing platform for 2,4,6-trinitrophenol detection. *Anal Chem*. 2014;86(15):7463–7470. doi:10.1021/ac5012014
24. Gu W, Yan Y, Zhang C, Ding C, Xian Y. One-step synthesis of water-soluble MoS<sub>2</sub> quantum dots via a hydrothermal method as a fluorescent probe for hyaluronidase detection. *ACS Appl Mater Interfaces*. 2016;8:11272–11279. doi:10.1021/acsami.6b01166
25. Yue Q, Chang S, Qin S, Li J. Functionalization of monolayer MoS<sub>2</sub> by substitutional doping: a first-principles study. *Phys Letters A*. 2013;377:1362–1367. doi:10.1016/j.physleta.2013.03.034
26. Tan H, Hu W, Wang C, et al. Intrinsic ferromagnetism in Mn-substituted MoS<sub>2</sub> nanosheets achieved by supercritical hydrothermal reaction. *Small*. 2017;13:1701389. doi:10.1002/smll.v13.39
27. Ren X, Ma Q, Fan H, et al. A Se-doped MoS<sub>2</sub> nanosheet for improved hydrogen evolution reaction. *Chem Commun*. 2015;51:15997. doi:10.1039/C5CC06847A
28. Kaur H, Bruno JG, Kumar A, Sharma TK. Aptamers in the therapeutics and diagnostics pipelines. *Theranostics*. 2018;8(15):4016, 4032. doi:10.7150/thno.25958
29. Chopra A, Shukla R, Sharma TK. Aptamers as an emerging player in biology. *Aptamers Synth Antibodies*. 2014;1(1):1–11.
30. Li JJ, Wang S, Wu C, et al. Activatable molecular MRI nanoprobe for tumor cell imaging based on gadolinium oxide and iron oxide nanoparticle. *Biosens Bioelectron*. 2016;86:1047–1053. doi:10.1016/j.bios.2016.07.044
31. Zheng S, Han J, Jin Z, et al. Dual tumor-targeted multifunctional magnetic hyaluronic acid micelles for enhanced MR imaging and combined photothermal-therapy. *Colloids Surf*. 2018;164:424–435. doi:10.1016/j.colsurfb.2018.02.005
32. Hao J, Song G, Liu T, Yang K, Cheng L, Liu Z. In vivo long-term biodistribution, excretion, and toxicology of PEGylated transition-metal dichalcogenides MS<sub>2</sub> (M = Mo, W, Ti) nanosheets. *Adv Sci*. 2017;4:1600160. doi:10.1002/advs.201600160
33. Jia Q, Ge J, Liu W, et al. A Magnetofluorescent carbon dot assembly as an acidic H<sub>2</sub>O<sub>2</sub>-driven oxygenator to regulate tumor hypoxia for simultaneous bimodal imaging and enhanced photodynamic therapy. *Adv Mater*. 2018;1706090. doi:10.1002/adma.201706090
34. Bates PJ, Laber DA, Miller DM, Thomas SD, Trent JO. Discovery and development of the G-rich oligonucleotide AS1411 as a novel treatment for cancer. *Exp Mol Pathol*. 2009;86:151–164. doi:10.1016/j.yexmp.2009.01.004
35. Dai Y, Zhang A, You J, Li J, Xu H, Xu K. Fabrication of AS1411 aptamer functionalized Gd<sub>2</sub>O<sub>3</sub>-based molecular magnetic resonance imaging (mMRI) nanoprobe for renal carcinoma cell imaging. *RSC Adv*. 2015;5:77204–77210. doi:10.1039/C5RA17211J

## International Journal of Nanomedicine

### Publish your work in this journal

The International Journal of Nanomedicine is an international, peer-reviewed journal focusing on the application of nanotechnology in diagnostics, therapeutics, and drug delivery systems throughout the biomedical field. This journal is indexed on PubMed Central, MedLine, CAS, SciSearch®, Current Contents®/Clinical Medicine,

Journal Citation Reports/Science Edition, EMBase, Scopus and the Elsevier Bibliographic databases. The manuscript management system is completely online and includes a very quick and fair peer-review system, which is all easy to use. Visit <http://www.dovepress.com/testimonials.php> to read real quotes from published authors.

Submit your manuscript here: <https://www.dovepress.com/international-journal-of-nanomedicine-journal>